INTERNATIONAL JOURNAL FOR NUMERICAL METHODS IN FLUIDS
Int. J. Numer. Meth. Fluids 2002; **38**:711–727 (DOI: 10.1002/fld.240)

A three-dimensional boundary layer scheme: stability and accuracy analyses

Jalil Horri-Naceur and Daniel Buisine*,†

Laboratoire de Mécanique de Lille (*L.M.L.*), *Bâtiment M3* (*Mécanique*),
Université des Sciences et Technologies de Lille, *59655 Villeneuve d'Ascq*, *France*

SUMMARY

We present a numerical scheme for the calculation of incompressible three-dimensional boundary layers (3DBL), designed to take advantage of the 3DBL model's overall hyperbolic nature, which is linked to the existence of wedge-shaped dependence and influence zones. The proposed scheme, explicit along the wall and implicit in the normal direction, allows large time steps, thus enabling fast convergence. In order to keep this partly implicit character, the control volumes for the mass and momentum balances are not staggered along the wall. This results in a lack of numerical viscosity, making the scheme unstable. The implementation of a numerical diffusion, suited to the local zone of influence, restores the stability of the boundary layer scheme while preserving second-order space accuracy. The purpose of this article is to present the analytical and numerical studies carried out to establish the scheme's accuracy and stability properties. Copyright © 2002 John Wiley & Sons, Ltd.

KEY WORDS: boundary layer; hyperbolic model; finite volume method; numerical stability; accuracy

NOMENCLATURE

(ξ_1, ξ_2)	non-orthogonal curvilinear coordinate system on a solid wall
$z, \Delta z$	space coordinate and grid size along local wall normal
$\mathbf{e_1}, \mathbf{e_2}$	local base vectors (cell sides) in (ξ_1, ξ_2) plane
i, j, k	node numbering indices in the ξ_1, ξ_2 and z directions
$\mathbf{W}$	relative velocity in rotating frame
$\mathbf{W_s}$	projection of relative velocity onto local (ξ_1, ξ_2) plane
W_z	Cartesian component of $\mathbf{W}$ in the z direction
w^1, w^2	contravariant components of $\mathbf{W_s}$
$U = w^1\lvert e_1\rvert, V = w^2\lvert e_2\rvert$	physical contravariant components of $\mathbf{W_s}$
ΔS	area of cell projection in local (ξ_1, ξ_2) plane
ΔV	volume of (momentum or mass) control domain

*Correspondence to: D. Buisine, LML, Bâtiment M3 (Mécanique), Université des Sciences et Technologies de Lille, 59655 Villeneuve D'Ascq Cedex, France.
†E-mail: daniel.buisine@univ-lille1.fr

Received February 2001
Revised July 2001

φ	general function of space coordinates
Φ_{edge}	discretized pressure term as a function of boundary layer edge velocity
Operators	
δ_m	difference in the ξ_m direction, e.g. $\delta_{1\varphi} \equiv \varphi(\mathbf{x}_{i+1,j,k}) - \varphi(\mathbf{x}_{i,j,k})$
μ_m	averaging in the ξ_m direction, e.g. $\mu_{1\varphi} \equiv \frac{1}{2}[\varphi(\mathbf{x}_{i,j,k}) + \varphi(\mathbf{x}_{i+1,j,k})]$

1. INTRODUCTION

The need for cost-effective prediction of flows of industrial interest leads to the consideration of the coupling of a boundary layer code with two types of fast-converging solvers: direct Euler and implicit Navier–Stokes.

The boundary layer scheme presented here is designed to take advantage of the overall hyperbolic behaviour of the 3DBL model. Indeed, while the 3DBL problem is locally parabolic along each streamline, the viscous diffusion along the local normal to the wall enforces a coupling among the streamlines going through that normal. This results [1, 2] in the existence of wedge-shaped dependence and influence zones bounded by the local normal and the outermost streamlines that cross it. This has prompted some authors [3, 4] to use a characteristics-based approach by performing finite-difference discretization along the local streamlines.

In order to give the present finite-volume scheme an explicit character along the wall while retaining the implicitness only along the normal, the flow variables on any point of the normal must depend only on nodes located either on the same normal or immediately upstream within its domain of dependence. Therefore, the control volumes we use for the mass and momentum balances are not staggered along the wall.

Unlike other space-marching methods, where a domain sweep by successive crosswise planes requires $\mathcal{O}(N^5)$ operations because of the large systems to be solved, the present scheme conserves the computational advantage of a 2D boundary layer model by marching downstream one cell column at a time. Finite-volume discretization leads to a block-tridiagonal system along each normal. The blocks are square matrices of order two, resulting in a much lower computational cost than with Navier–Stokes solvers: a complete sweep of the computational domain requires only $\mathcal{O}(N^3)$ operations.

Since the pressure is part of the data, large time steps can be used without stability conditions of the Courant–Friedrichs–Levy (CFL) type. However, the use of control volumes that are unstaggered along the wall generates oscillations in the solution. Such perturbations, often referred to as 'checkerboard modes' [5], are also encountered in unstaggered-grid discretizations of the full Navier–Stokes equations [6]. In order to remedy these stability problems, we introduce diffusion operators specifically adapted to the configuration of the local dependence and influence domains with respect to the mesh.

In this paper, we present the analyses and numerical tests which have allowed us to establish the stability and accuracy properties of the boundary layer scheme. After a brief description of the discretization and the implementation of numerical diffusion, we present a linear stability analysis whose purpose is to quantify the disturbance amplification factor for each numerical diffusion mode.

Sections 4 and 5 deal with the assessment of the scheme's accuracy, starting with an equivalent-equation analysis of the truncation errors. The results of that analysis are corrob-

orated by the validation of the computational code using a class of solutions of the laminar boundary layer equations. Self-similar laminar boundary layers [7, 8] governed by ordinary differential equations (ODEs) provide reference solutions which are used to directly compute the discretization errors. This numerical check confirms the scheme's second-order space accuracy. The last section presents a turbulent Ekman layer calculation, showing a satisfactory level of agreement between our numerical results and the available experimental data.

2. BOUNDARY LAYER SCHEME

2.1. Local equations in relative movement

Since the aim is to predict turbomachinery flows, the local equations are cast in a rotating frame of reference. The fluid is assumed incompressible, and the external high-Reynolds number flow is governed by the Euler equations. The normal pressure gradient is known, and assumed to be zero since wall curvature is neglected. This obviates the need for a momentum equation in the z direction normal to the wall. In keeping with boundary layer assumptions, viscous diffusion is only accounted for along the normal.

The momentum equation, in a plane locally parallel to the wall, reads:

$$\frac{\partial \mathbf{W_s}}{\partial t} + \nabla_S \cdot (\mathbf{W_s} \otimes \mathbf{W_s}) + \frac{\partial}{\partial z}(W_z \mathbf{W_s}) + 2\boldsymbol{\omega_o} \times (\mathbf{W_s} - \mathbf{W_s^e}) - \frac{\partial}{\partial z}\left(\nu \frac{\partial \mathbf{W_s}}{\partial z}\right) - \nabla_S \cdot (\mathbf{W_s^e} \otimes \mathbf{W_s^e}) - \frac{\partial}{\partial z}(W_z^e \mathbf{W_s^e}) = 0 \tag{1}$$

where ω_o is the rotation vector of the moving coordinate frame. The relative velocity $\mathbf{W}$ is split into a vector $\mathbf{W_s}$ parallel to the wall and a normal component W_z with a similar decomposition applying to the boundary layer edge velocity $\mathbf{W}^e$. In the above equation, the pressure gradient is replaced by its expression as a function of the edge velocity $\mathbf{W_s^e}$, derived from the Euler equation.

The continuity equation can be written as follows, based on the decomposition of $\mathbf{W}$:

$$\nabla \cdot \mathbf{W_s} + \frac{\partial W_z}{\partial z} = 0 \tag{2}$$

2.2. Space discretization

A finite-volume discretization is used, whereby the boundary layer equations are integrated over a structured mesh of hexahedral cells. These are stacked into prismatic columns bounded by the local normal to the wall and the quadrangles formed on the wall by the intersection of the ξ_1 and ξ_2 non-orthogonal curvilinear coordinate lines. The ξ_1 and ξ_2 coordinates are chosen to be identical to the (i, j) node numbering in the plane locally parallel to the wall. For each station in z, the momentum balance is written over a control domain $\mathscr{D}_{qm}$ made up of two vertically adjacent half-cells (see Figure 1).

The discretized momentum balance over $\mathscr{D}_{qm}$ involves linear terms (time derivative, Coriolis term, viscous diffusion) along with flux terms:

$$\mu_1\mu_2\mu_3 \frac{\partial \mathbf{W_s}}{\partial t}\Delta V + \mathbf{A} \cdot \mathbf{W_s} + \mu_3[\delta_1\mu_2(\mathbf{W_s} w^1 \Delta S \Delta z) + \delta_2\mu_1(\mathbf{W_s} w^2 \Delta S \Delta z)] + \Phi_{\text{edge}} = 0 \tag{3}$$

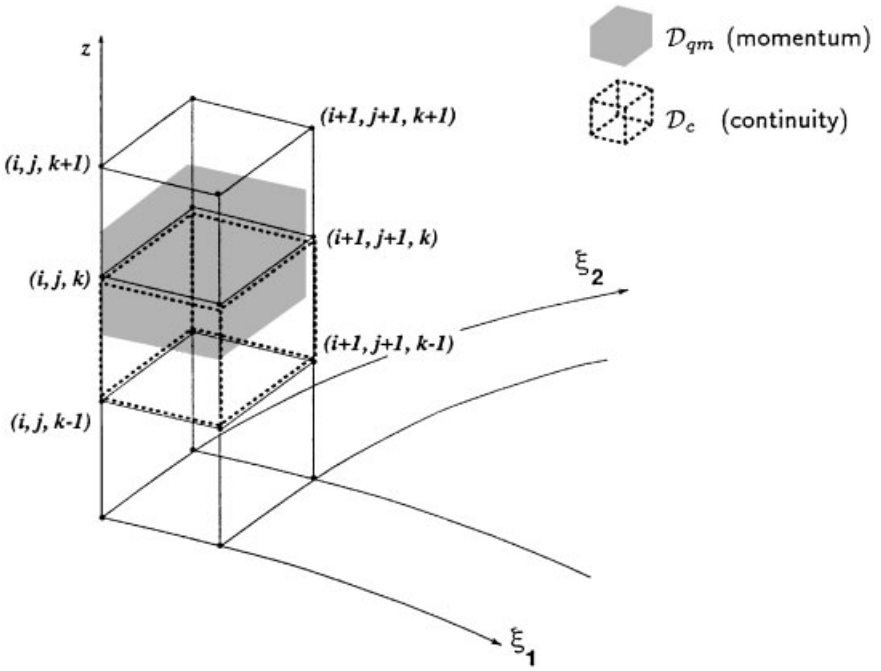

Figure 1. Grid and control volumes.

where

$$\mathbf{A} \cdot \mathbf{W_s} = 2\mu_1\mu_2\mu_3(\boldsymbol{\omega}_0 k \times \mathbf{W_s})\Delta V + \delta_3(W_z\mathbf{W_s})\Delta S - \delta_3\left(\frac{v}{\Delta z}\mu_1\mu_2\delta_3\mathbf{W_s}\right)\Delta S$$

Similarly, the discretized mass balance over a mesh cell (control domain $\mathscr{D}_c$) reads:

$$\mu_3[\delta_1\mu_2(w^1\Delta S\Delta z) + \delta_2\mu_1(w^2\Delta S\Delta z)] + \delta_3(\Delta S W_z) = 0 \tag{4}$$

In the following, we replace the contravariant components of $\mathbf{W_s}$ with their physical equivalents U and V.

2.3. Time discretization

In the two-level time discretization, a parameter, θ, is used to write the momentum equation at an intermediate time level $n + \theta$. We use the following linearized form to approximate nonlinear convective terms:

$$\widehat{UV}^{n+\theta} = (1 - 2\theta)U^nV^n + \theta(U^nV^{n+1} + U^{n+1}V^n); \quad 0 < \theta \leqslant 1 \tag{5}$$

In agreement with the boundary layer assumptions and the incompressibility of the fluid, the continuity equation determines the normal velocity component W_z instead of the pressure. The mass balance (Equation (4)), combined with the non-porous wall condition, yields the cell-centered W_z component, which is substituted into the momentum equation. After linearization

of Equation (3), a matrix form of the momentum balance is derived:

$$\sum_{\alpha,\beta,\gamma} \begin{bmatrix} C_x^u(U^n,V^n) & C_x^v(U^n,V^n) \\ C_y^u(U^n,V^n) & C_y^v(U^n,V^n) \end{bmatrix}_{\alpha,\beta,\gamma} \begin{Bmatrix} U \\ V \end{Bmatrix}_{\alpha,\beta,\gamma}^{n+1} = \begin{Bmatrix} S_x(U^n,V^n) \\ S_y(U^n,V^n) \end{Bmatrix}_{i,j,k} \tag{6}$$

with $\alpha \in \{i, i+1\}$; $\beta \in \{j, j+1\}$; $\gamma \in \{k-1, k, k+1\}$, where indices (i,j,k) refer to the current cell's position in the (ξ_1, ξ_2, z) directions. For all mesh cells contained in the (i,j) column, the system's unknowns are the velocity components at the 'downstream' node of the cell, here $(U,V)_{i+1,j,k}^{n+1}$ or $(U,V)_{i+1,j+1,k}^{n+1}$ depending on the sign of w^2. The coordinate system is chosen so that $w^1 > 0$.

The fact that the mass and momentum control volumes are only staggered in the z direction preserves the hyperbolic and explicit character of the model along the wall. The scheme can thus be considered explicit along ξ_1 and ξ_2, and implicit along z. This partly implicit character allows large time steps to be used. On the other hand, the unstaggered arrangement of the control domains $\mathscr{D}_c$ et $\mathscr{D}_{qm}$ parallel to the wall results in a lack of numerical viscosity in the ξ_1 and ξ_2 directions, unlike usual schemes. This gives rise to instabilities in the solution, with oscillatory disturbances that spread across the local zone of influence. In order to restore the scheme's stability, we implement numerical diffusion operators which we define according to the influence domain, hence the local velocity vector.

2.4. Implementation of numerical diffusion

As in other solution methods [9] where different schemes are used from one wall normal to another, several modes of numerical diffusion are devised [10, 11] depending on the direction of the local velocity vector with respect to the current cell's diagonal.

The choice of the diffusion operators originates in our analysis [11] of the stability behaviour of the scheme: indeed, the latter is found to be stable only when the local velocity vector, $\mathbf{W_s}$, is close enough to the cell's diagonal.

When $\mathbf{W_s}$ gradually moves away from the diagonal, system (Equation (6)), intended for the calculation of the velocity components at the so-called downstream node, becomes increasingly unstable. Thus, it becomes necessary to lend more weight to the other node located on the cell side through which $\mathbf{W_s}$ passes. Therefore, system (6) has to be rewritten so that at least one of the unknown (U,V) components is located at $(i+1, j+\zeta)$ or $(i+\zeta, j+1)$, depending on the cell side crossed by $\mathbf{W_s}$.

Based on numerical experience, we choose to keep the weighting factor fixed, $\zeta = 1/2$, so that the system unknowns are midpoint values of the crossflow component (cases II and IV in Figure 2) or of both components (cases III and V). (By crossflow component we mean the one that is not dominant, i.e. $\min(U,V)$). These choices will be validated by the stability analysis (see Section 3).

Each diffusion mode has a range of applicability defined in terms of $\mathscr{R} = [(w^2)/(w^1)]$, so that the various cases depicted in Figure 2, as well as their mirror images with respect to the ξ_1 axis, are swept as $\mathscr{R}$ varies in $[-\infty, \infty]$. It is worth noting that, in the present scheme, several numerical diffusion modes can be used along the same local normal, to allow for skewed velocity profiles along local wall normals.

In order to describe the actual diffusion operators, we consider for example the flux terms in Equation (3) which correspond to the downstream cell side aligned with the ξ_2 direction.

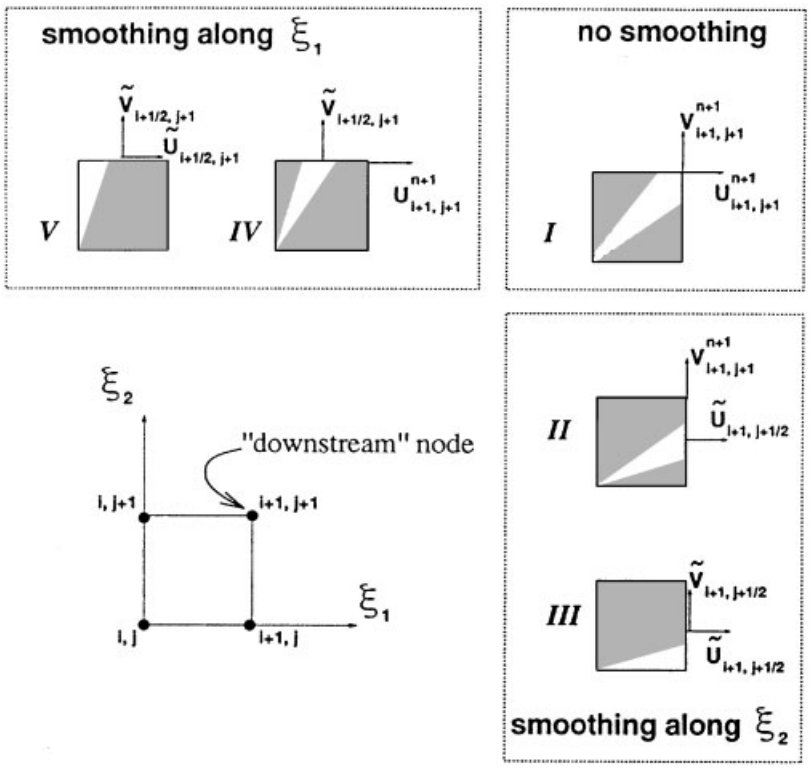

Figure 2. Introduction of numerical diffusion: different possible cases.

These terms are linearized using a relationship of Equation (5) form to derive the linear system (6):

$$\mu_2(\mathbf{W_s} w^1 \Delta S \Delta z)_{i+1} = a_j \mathbf{W}_{\mathbf{s}_{i+1,j}} + a_{j+1} \mathbf{W}_{\mathbf{s}_{i+1,j+1}}$$

The midpoint velocity is introduced by means of an identity:

$$a_j \mathbf{W}_{\mathbf{s}_{i+1,j}} + a_{j+1} \mathbf{W}_{\mathbf{s}_{i+1,j+1}} = \frac{1}{2}(a_j + a_{j+1})(\mathbf{W}_{\mathbf{s}_{i+1,j}} + \mathbf{W}_{\mathbf{s}_{i+1,j+1}}) + \frac{1}{2}(a_{j+1} - a_j)(\mathbf{W}_{\mathbf{s}_{i+1,j+1}} - \mathbf{W}_{\mathbf{s}_{i+1,j}}) \quad (7)$$

The first term on the right-hand side involves the midpoint velocity, $\tilde{\mathbf{W}}_\mathbf{s}$, evaluated at the $n+1$ time level, while the second term, which is two orders higher, is taken at time step n. Transformations such as Equation (7) result in modified systems whose unknowns are among $\{U, V, \tilde{U}, \tilde{V}\}$.

As soon as the modified systems are solved on two adjacent cells, the resulting components are linearly interpolated to yield the velocity at the dowstream node.

We hereafter present the most relevant part of the analytical and numerical checks carried out to assess the scheme's stability and accuracy prior to its use in the calculation of industrial turbulent-flow test cases.

3. LINEAR STABILITY ANALYSIS

In this section, we investigate the scheme's stability properties by evaluating the amplification factor of its associated operator in all the cases illustrated by Figure 2.

Given the behaviour [2, 1] of the three-dimensional boundary layer model with respect to the (x, y) coordinates, the stability analysis is simplified if we consider a two-dimensional film flow, which exhibits the same properties as a 3DBL as far as fluctuation transmission is concerned.

In this analysis, the mesh is assumed orthogonal, with constant Δx, Δy spacings.

The momentum equation for a 2D film flow, averaged through the film's thickness, reads:

$$\frac{\partial \mathbf{W}}{\partial t} + \boldsymbol{\nabla} \cdot (\mathbf{W} \otimes \mathbf{W}) + 2\omega_o \times \mathbf{W} + \boldsymbol{\nabla}\left(\frac{P}{\rho} - \frac{\omega_o^2 r^2}{2}\right) + K\mathbf{W} = 0 \tag{8}$$

where $\mathbf{W}$ is the relative velocity in the (x, y) plane, P is the pressure, and K the friction coefficient.

In the case of the 2D film flow, we shall establish that the proposed diffusion operators ensure stability of the finite-volume scheme. The use of these operators has been observed numerically to have the same stabilizing effect on the 3D boundary layer scheme, which is unstable in its basic form without explicitly added numerical diffusion.

3.1. *Description of the fluctuations*

Given the convective nature of the oscillations encountered when the scheme's stability limits are transgressed, a classical, Von Neumann-like decomposition of the solution into Fourier modes would lead to an exceedingly optimistic assessment of the scheme's stability.

Therefore, in the present study, the function space is expanded to include complex-wave-number disturbances, which are superimposed on an assumed steady-state solution to model the actual oscillations. Thus, the magnitude variation coefficients, denoted below by a and b, may be positive, to account for error accumulation during the sweeping of the computational domain, or they may be negative, to simulate a locally decreasing error brought about by unsuitable or varying inlet boundary conditions.

In the following, $\underline{w}$ represents the magnitude of the disturbance w at an arbitrarily chosen reference point R. If the origin of the (x, y) coordinate system is set at R, the disturbed solution at time step n reads:

$$\begin{Bmatrix} U^n \\ V^n \end{Bmatrix} = \begin{Bmatrix} U^o \\ V^o \end{Bmatrix} + \begin{Bmatrix} \underline{u}^n \\ \underline{v}^n \end{Bmatrix} e^{\mathrm{i}\mathbf{k}\cdot\mathbf{x}} = \begin{Bmatrix} U^o \\ V^o \end{Bmatrix} + \begin{Bmatrix} \underline{u}^n \\ \underline{v}^n \end{Bmatrix} e^{(a+\mathrm{i}\omega_x)x+(b+\mathrm{i}\omega_y)y} \tag{9}$$

where ω_x and ω_y are the real wavenumbers of the disturbance.

3.2. Local amplification factor

The local character of this stability analysis, in the sense that boundary conditions are not taken into account, is consistent with the fact that numerical viscosity is implemented locally, using operators that differ from one point to another in the domain.

Substituting the disturbed velocities at steps n and $n+1$, as defined by Equation (9), into the matrix form of the momentum balance, leads to the derivation of a transformation operator $[G]$, represented by a square matrix of order two, which links two successive states of the disturbance:

$$\begin{Bmatrix} \underline{u}^{n+1} \\ \underline{v}^{n+1} \end{Bmatrix} = [G(U^o, V^o, \omega_x, \omega_y, a, b)] \begin{Bmatrix} \underline{u}^{n} \\ \underline{v}^{n} \end{Bmatrix} = \rho_o e^{\mathrm{i}\Delta\phi} \begin{Bmatrix} \underline{u}^{n} \\ \underline{v}^{n} \end{Bmatrix}$$

where ρ_o is the spectral radius of matrix $[G]$, defined by: $\rho_o = |\lambda_m| = \sup_{i=1,2} |\lambda_i|$ with the eigenvalues of $[G]$ represented by λ_i.

While for spatially growing waves a spectral radius ρ_o less than unity indicates that the disturbance is carried away downstream, for spatially decaying waves the correct amplification factor is the one seen by an observer moving downstream with the wave. In the latter case, in order to compute the actual amplification factor, the phase shift $\Delta\phi$, brought in by the operator $[G]$, is used to determine the distance travelled by the wave during one time step and the corresponding magnitude correction:

$$\frac{\rho}{\rho_o} = e^{(a\bar{U}+b\bar{V})\Delta t} \tag{10}$$

where $\bar{U}$ and $\bar{V}$, the components of the wave transport velocity, are evaluated using: $\Delta\phi = -(\omega_x\bar{U} + \omega_y\bar{V})\Delta t$ and assuming that $\bar{V}/\bar{U} = \underline{V}^o/\underline{U}^o$.

3.3. Stability analysis results

We present some of the results obtained in the dimensionless parameter range described in Table I. For each numerical diffusion mode, and for each combination of the θ and $K\Delta t$ parameters, the variations of the transformation matrix's spectral radius, ρ, are synthesized by a three-dimensional graphical representation of the function:

$$\sup_{C,\omega_x,\omega_y,a,b} \rho = f(\Delta y/\Delta x, V^o/U^o)$$

Figures 3 to 5 display the stability zones of the different numerical diffusion modes.

As expected, the stability zone for mode I without numerical diffusion is confined to a narrow region where the velocity vector is close to the mesh cell's diagonal (between contour lines marked A and B in Figure 3). Accordingly, in the boundary layer code we only use mode I for $\mathscr{R}_1 \leqslant \mathscr{R} \leqslant 1/\mathscr{R}_1$, with $\mathscr{R}_1 \approx 0.95$ typically.

When one or both velocity components undergo numerical diffusion, the stability zones are notably widened. Actually, the union of stability zones associated with modes I, III and V would cover all the possible directions of the velocity vector. However, modes II and IV are retained because they entail less numerical viscosity than modes III and V, where diffusion operators affect both velocity components (see Table II).

Table I. Dimensionless parameters for the linear stability analysis.

Parameter	Range of variation
Courant number	$C = U\Delta t/\Delta x \in [0.0; 50.0]$
Viscous friction	$K\Delta t \in [0.001; 0.1]$
Time shift parameter $(n + \theta\Delta t)$	$\theta \in [0.0; 1.0]$
Cell aspect ratio	$\Delta y/\Delta x \in [0.001; 10.0]$
Velocity vector direction in local coordinates	$V^o/U^o \in [0.001; 10.0]$
Disturbance wavelength spectrum bounds	$\Lambda_x/\Delta x, \Lambda_y/\Delta y) \in [2; 200]^2$
Disturbance magnitude variation coefficients	$(e^{a\Delta x}, e^{b\Delta y}) \in [0.75; 1.5]^2$

Table II. Ranges of applicability of numerical diffusion modes.

$\mathscr{R} \equiv (V/\Delta y)/(U/\Delta x)$	
Range of $\mathscr{R}$	Numerical diffusion mode
$0 \leqslant \mathscr{R} < \mathscr{R}_1$	III
$\mathscr{R}_1 \leqslant \mathscr{R} < \mathscr{R}_2$	II
$\mathscr{R}_2 \leqslant \mathscr{R} < 1/\mathscr{R}_2$	I
$1/\mathscr{R}_2 \leqslant \mathscr{R} < 1/\mathscr{R}_1$	IV
$\mathscr{R} \geqslant 1/\mathscr{R}_1$	V
Typically, $\mathscr{R}_1 = 0.6$ and $\mathscr{R}_2 = 0.95$	

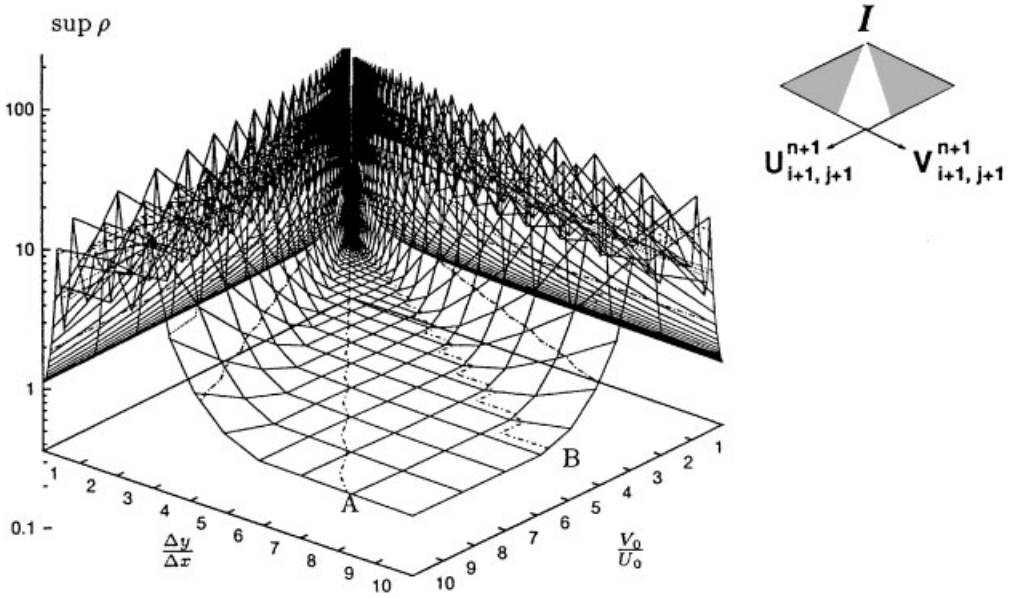

Figure 3. Stability zone without numerical diffusion (mode I).

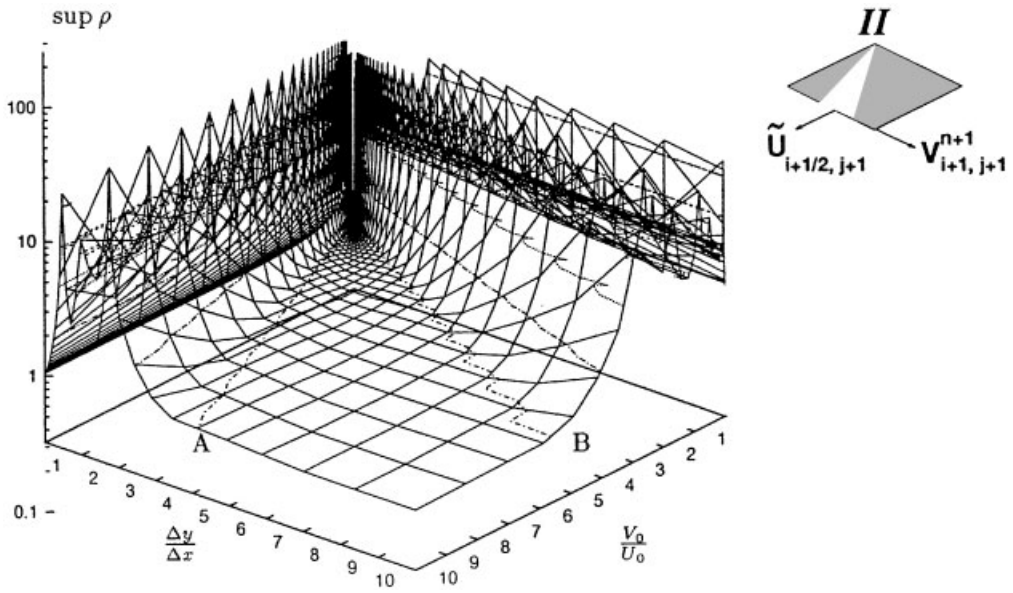

Figure 4. Stability zone; numerical diffusion on component U along ξ_2 (mode II).

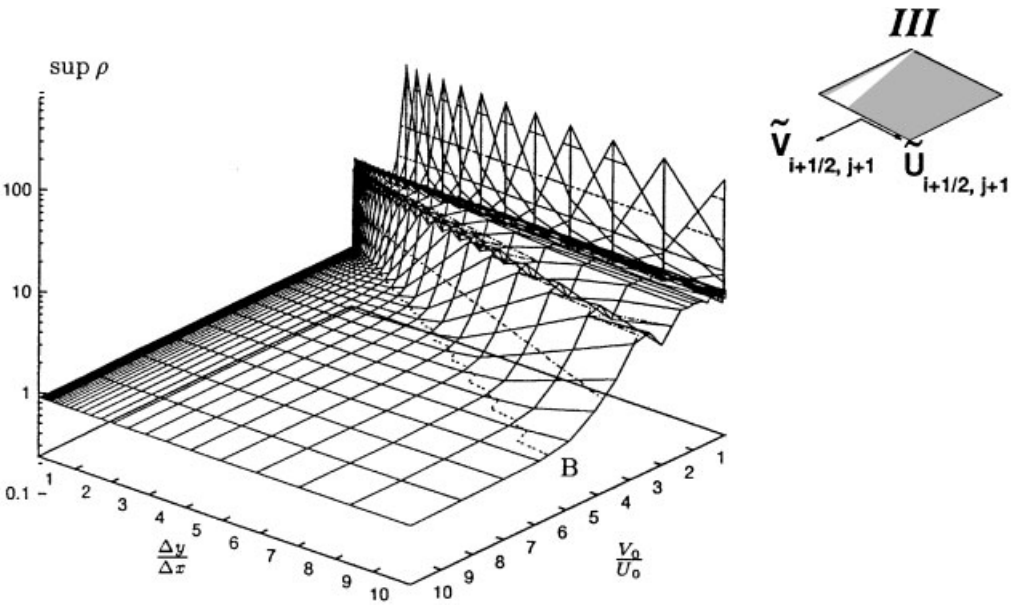

Figure 5. Stability zone; numerical diffusion on components U and V along ξ_2 (mode III).

Having shown the effectiveness of the various numerical diffusion modes in enforcing stability, we now present a consistency analysis of the scheme, based on a Taylor-expansion truncation error analysis, often referred to as the equivalent (or modified) equation method.

4. ANALYTICAL CONSISTENCY STUDY

In order to determine the truncation error, focussing mainly on space accuracy, we hereafter use a representation of the solution based on Taylor expansions about the centre R of the momentum control domain, $\mathscr{D}_{qm}$. The nodal velocity components are substituted into the discrete momentum balance. Once the exact PDE terms are collected, all the remaining terms represent the discretization (or truncation) error.

For instance, in projection over the x direction, the following equivalent equation is derived:

$$
\begin{aligned}
&\frac{\partial U}{\partial t} - 2\omega_o V - \nu\frac{\partial^2 U}{\partial z^2} + U\frac{\partial U}{\partial x} + V\frac{\partial U}{\partial y} + W\frac{\partial U}{\partial x} + \Phi_x(\mathbf{W}_{\mathbf{s}}^{e}) \\
&\quad \left.\begin{aligned}
&+\frac{\Delta x^2}{8}\Bigg(\frac{\partial U}{\partial x}\,\frac{\partial^2 U}{\partial x^2} + \frac{\partial U}{\partial y}\,\frac{\partial^2 V}{\partial x^2} + 2\,\frac{\partial U}{\partial x}\,\frac{\partial^2 V}{\partial x\partial y} + 2\,\frac{\partial V}{\partial x}\,\frac{\partial^2 U}{\partial x\partial y} \\
&\qquad + \frac{2}{3}\,U\frac{\partial^3 U}{\partial x^3} + \frac{1}{3}\,U\frac{\partial^3 V}{\partial x^2\partial y} + \frac{1}{3}\,V\frac{\partial^3 U}{\partial x^2\partial y} + W\frac{\partial^3 U}{\partial x^2\partial z} \\
&\qquad + \frac{\partial}{\partial t}\,\frac{\partial^2 U}{\partial x^2} - 2\omega_o\,\frac{\partial^2 V}{\partial x^2} + p(U,V)\Bigg) \\
&+\frac{\Delta y^2}{8}\Bigg(\frac{\partial U}{\partial x}\,\frac{\partial^2 U}{\partial y^2} + 4\,\frac{\partial U}{\partial y}\,\frac{\partial^2 U}{\partial x\partial y} + \frac{\partial U}{\partial y}\,\frac{\partial^2 V}{\partial y^2} \\
&\qquad + 2U\frac{\partial^3 U}{\partial x\partial y^2} + \frac{1}{3}U\frac{\partial^3 V}{\partial y^3} + \frac{1}{3}V\frac{\partial^3 U}{\partial y^3} + W\frac{\partial^3 U}{\partial y^2\partial z} \\
&\qquad + \frac{\partial}{\partial t}\,\frac{\partial^2 U}{\partial y^2} - 2\omega_o\,\frac{\partial^2 V}{\partial y^2} + q(U,V)\Bigg) \\
&+\frac{\Delta z^2}{8}\Bigg(-\frac{\partial V}{\partial y}\,\frac{\partial^2 U}{\partial z^2} + \frac{\partial U}{\partial y}\,\frac{\partial^2 V}{\partial z^2} + \frac{\partial U}{\partial z}\,\frac{\partial^2 W}{\partial z^2} \\
&\qquad + 4\,\frac{\partial U}{\partial z}\,\frac{\partial^2 U}{\partial x\partial z} + 2\,\frac{\partial U}{\partial z}\,\frac{\partial^2 V}{\partial y\partial z} + 2\,\frac{\partial V}{\partial z}\,\frac{\partial^2 U}{\partial y\partial z} \\
&\qquad + 2U\frac{\partial^3 U}{\partial x\partial z^2} + U\frac{\partial^3 V}{\partial y\partial z^2} + V\frac{\partial^3 U}{\partial y\partial z^2} + \frac{1}{3}\,U\frac{\partial^3 W}{\partial z^3} + \frac{4}{3}\,W\frac{\partial^3 U}{\partial z^3} \\
&\qquad + \frac{\partial}{\partial t}\,\frac{\partial^2 U}{\partial z^2} - 2\omega_o\,\frac{\partial^2 V}{\partial z^2} + r(U,V)\Bigg) + s(U,V)
\end{aligned}\right\}\text{truncation error} \\
&\quad + \mathscr{E}(\Delta t, \Delta t^2) \\
&\qquad = 0
\end{aligned}
\tag{11}
$$

where the Δx, Δy, and Δz spacings of the orthogonal mesh are assumed uniform but not necessarily equal, and only laminar flow is considered, hence a uniform viscosity.

The exact PDE appears, including the $\Phi_x(\mathbf{W}_\mathbf{s}^e)$ component of the pressure term written as a function of the edge velocity, while the additional terms are second-order space truncation errors, among which $p(U,V)$, $q(U,V)$, $r(U,V)$, and $s(U,V)$ vary according to the numerical diffusion operator used.

We now present a truncation error study carried out by comparing numerical results with a class of boundary layers, governed by ordinary differential equations (ODEs).

5. NUMERICAL ACCURACY CHECKS

The existence of reference solutions for self-similar laminar boundary layers enables truncation errors to be quantified directly as the difference between these solutions and the results computed using the proposed scheme.

5.1. Falkner–Skan/Cooke boundary layers

Falkner–Skan ODEs [7] exactly describe boundary layers whose edge velocity varies in the streamwise direction according to a power law.

The availability of a solution for the crosswise component makes the accuracy analysis possible for three-dimensional Falkner–Skan/Cooke boundary layers [8]. The code has thus been validated for boundary layers developing on swept flat planes with a pressure gradient normal to the leading edge. Under the infinite-span hypothesis, the (U_e, V_e) edge velocity components in the (x, y) coordinate system linked to the plate's edge are given by:

$$U_e = U_\infty x^m; \quad V_e = \text{const.} \tag{12}$$

The profiles of the U and V components are described by the Falkner–Skan/Cooke equations:

$$U(x,z) = U_e(x) \cdot F'(Z); \quad V(x,z) = V_e(x) \cdot G(Z) \tag{13}$$

where G, F, and the derivatives F', F'', F''' satisfy the following ODEs:

$$F''' + FF'' + \beta(1 - F'^2) = 0; \quad G'' + FG' = 0 \tag{14}$$

with

$$Z = z[(m+1)U_e/2\nu x]^{\frac{1}{2}}; \quad \beta = 2m/(m+1)$$

The boundary conditions on F and G are as follows:

$$F(0) = F'(0) = 0; \quad \lim_{Z\to\infty} F'(Z) = 1$$

$$G(0) = 0; \quad \lim_{Z\to\infty} G(Z) = 1$$

A finite-difference discretization, on a grid about 10 times finer than that used for actual boundary layer computations, was used to provide solutions of the ODEs accurate enough to be used as reference in computing truncation errors. In boundary layer computations, these

numerically obtained velocity profiles were used as inlet boundary conditions. Everywhere else in the domain, the initial conditions were deliberately offset.

In the following, we shall call 'error' the root-mean-square (RMS) norm, along a wall normal, of the differences between the theoretical solution and the one obtained using the boundary layer scheme:

$$\varepsilon_{i,j,n} = \frac{1}{N_z}\frac{1}{U_{\text{ref}}}\left[\sum_{k=1}^{N_e}(U_{\text{num}} - U_{\text{theo}})^2_{i,j,k,n}\right]^{\frac{1}{2}} = \|U_{\text{num}} - U_{\text{theo}}\|$$

where U_{ref} is the streamwise component of the local edge velocity. In addition, we shall refer by 'residual error' to the steady-state value (when there exists one) towards which $\varepsilon_{i,j,n}$ asymptotically tends as the calculation proceeds. These error norms are used hereafter to evaluate space truncation errors.

5.2. *Influence of the normal mesh spacing*

In order to check the second-order accuracy in Δz, we compare the residual errors obtained by computing the same flow on three grids defined as follows:

(i) the finest grid, refined near the wall by means of a geometrical progression, comprises 100 cells in z, with a size ratio of 25 between the first and last cells;
(ii) the medium grid is obtained by discarding every other node from the finest grid;
(iii) the coarse grid is obtained from the medium one in the same way.

Given the local ratio of the finest grid's geometrical sequence, $r = 25^{1/99} \approx 1.033$, the mesh size ratios between the grids are:

(i) $f^* \approx 2,033$ between the medium and the finest grids;
(ii) $f^{**} \approx 2,067$ between the coarse and the medium grids.

Figure 6 illustrates the time history of the error. The second-order accuracy of the scheme in Δz is confirmed by the ratio of the residual errors obtained with the three grids. Indeed, the errors are found to be in a ratio very close to 4:

(i) medium vs fine grid: $\varepsilon_M/\varepsilon_F \approx 4,091$;
(ii) coarse vs medium grid: $\varepsilon_C/\varepsilon_M \approx 4,019$.

The fact that doubling the Δz grid spacing almost exactly quadruples the truncation error clearly indicates that the Δz^2 term dominates this error. Preliminary tests with variable Δx and constant Δz have confirmed this interpretation, since they did not exhibit significant variations of the error.

We hereafter describe the method used to decouple the Δx and Δz errors and display the Δx order of accuracy.

5.3. *Influence of the streamwise grid spacing*

Starting from the assumption that the whole spatial truncation error is encompassed in the second-order terms of the equivalent equation, we express the discretization error in the

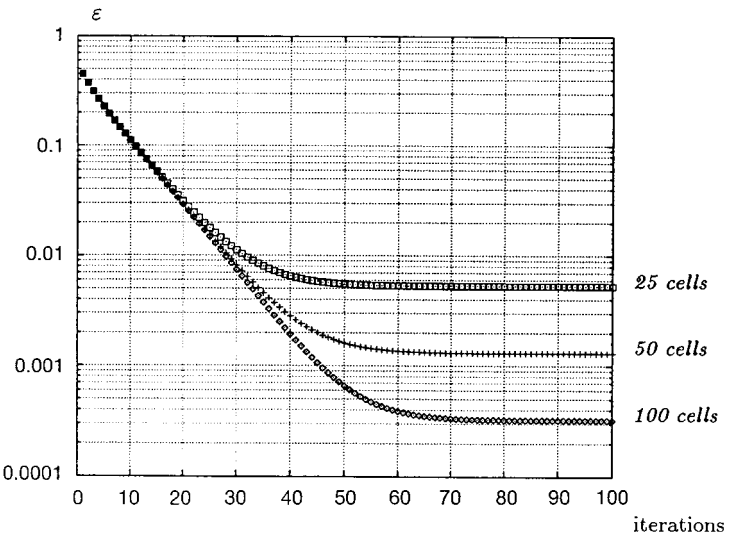

Figure 6. Effect of doubling normal grid spacing Δz on truncation error.

following polynomial form:

$$U_{\text{num}} - U_{\text{theo}} = f\Delta z^2 + g\Delta x^2 + h\Delta y^2 + \varepsilon_{\text{rnd}} \tag{15}$$

where f, g and h are functions of (x, y, z, t) and ε_{rnd} is the random roundoff error.

Let U_1, U_2 and U_3 be solutions obtained for the same flow on three meshes whose normal spacing Δz is identical while their streamwise cell sizes Δx_1, Δx_2 and Δx_3 are such that $\Delta x_3 = 2\Delta x_2 = 4\Delta x_1$. The error variation between a couple of numerical solutions can be written:

$$U_2 - U_1 = g(\Delta x_2^2 - \Delta x_1^2) = 3g\Delta x_1^2 \tag{16}$$

Similarly, we can state:

$$U_3 - U_2 = g(\Delta x_3^2 - \Delta x_2^2) = 12g\Delta x_1^2 \tag{17}$$

Thus, the ratio of the norms of *error differences* between solutions, $\varepsilon_{32} = \|U_3 - U_2\| = 12\|g\|\Delta x_1^2$ on one hand, and $\varepsilon_{21} = \|U_2 - U_1\| = 3\|g\|\Delta x_1^2$ on the other hand, can be expected to be very close to 4.

Figure 7 illustrates the result of a comparison carried out, following the procedure described above, between three numerical solutions obtained by doubling the streamwise grid size Δx. In such conditions, the ratio between the residual error differences ε_{32} and ε_{21} is found to be 3,97. The second-order accuracy in Δx is thus clearly established.

6. TURBULENT FLOW ON A ROTATING DISC

One of the turbulent-flow test cases computed using the present scheme is briefly presented for completeness.

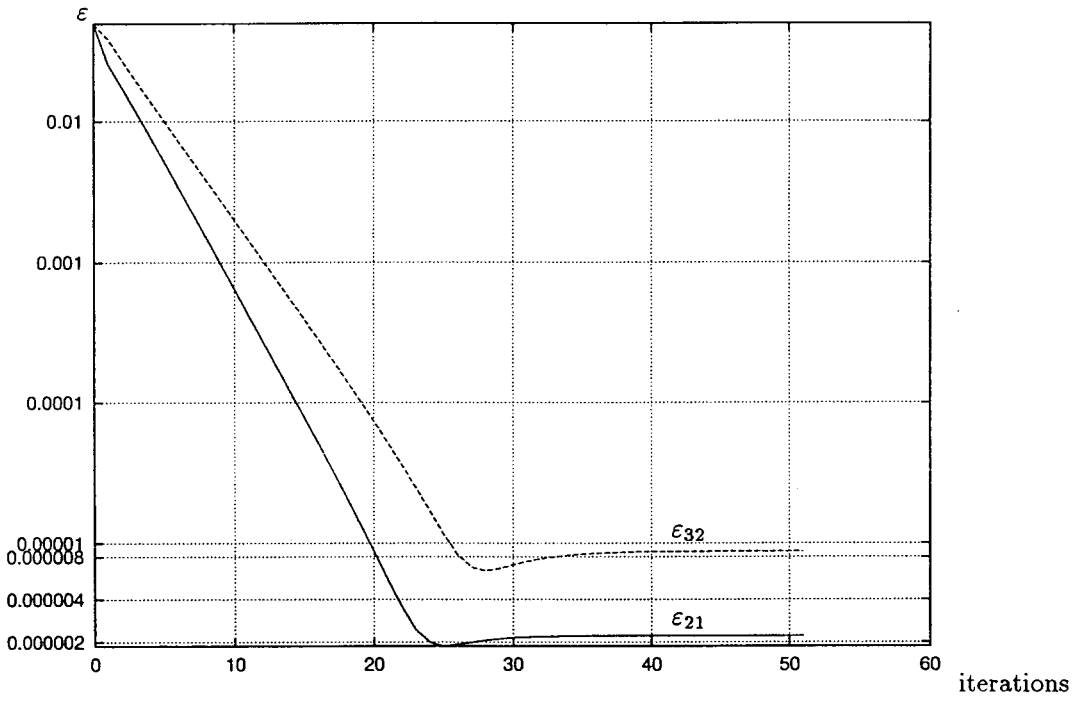

Figure 7. Variations of truncation error when Δx is doubled.

The flow of air over a one-metre diameter aluminium disc, rotating at frequencies up to 1500 rpm, was investigated experimentally by Littell and Eaton [12].

Figure 8 enables a comparison between our numerical relative velocity profiles and the experimental ones, based on the Reynolds number $Re = \Omega R^2/v$, where R is the current radial position, v the kinematic viscosity of the fluid, and Ω the angular velocity.

The agreement between numerical and experimental results is rather good, especially considering that the computations were performed using a simple algebraic (mixing-length) turbulence model which is notoriously inadequate for flows with a marked three-dimensional character, i.e. skewed velocity profiles.

7. CONCLUSION

A numerical scheme has been developed for the solution of the local three-dimensional boundary layer equations with the aim of exploiting the overall hyperbolic nature of the problem to solve explicit block-tridiagonal systems in each cell column considered independently. In order to fulfil this requirement, the proposed scheme does not entail staggering the continuity and momentum control volumes along the wall, unlike most frequently used techniques.

To cure the resulting instability problems, we implement a minimal amount of numerical viscosity depending on the shape of local dependence and influence zones. The latter are

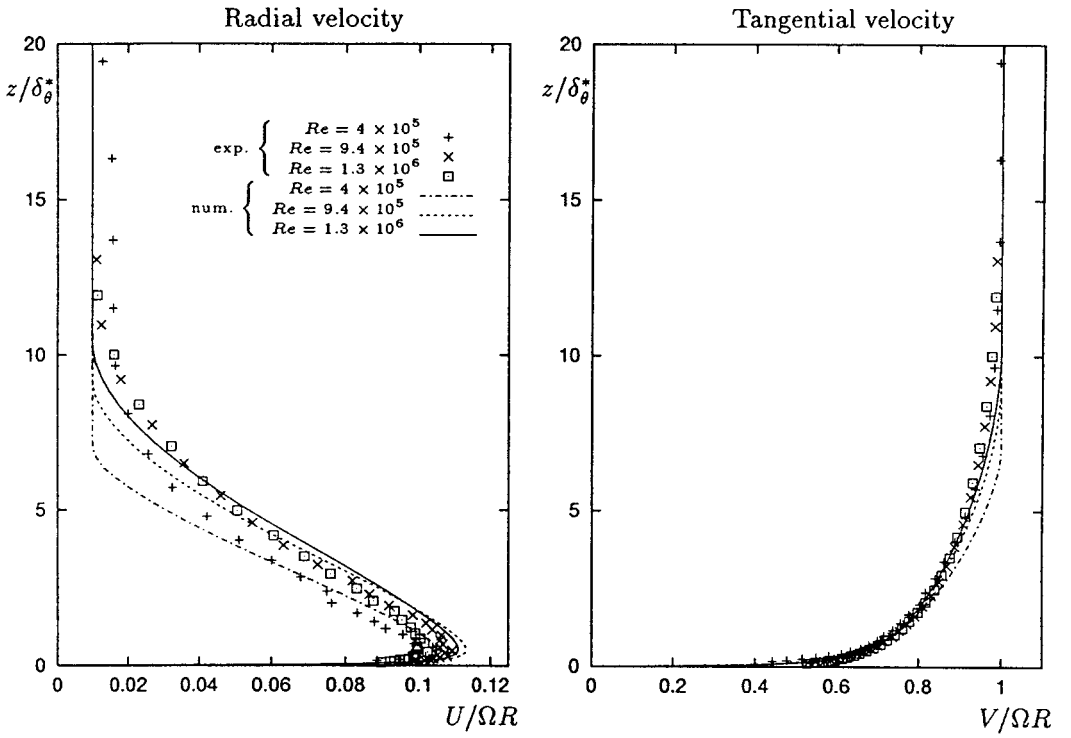

Figure 8. Rotating disc flow: comparison between numerical and experimental velocity profiles.

determined by the computed velocity field, which enables the adaptation of the numerical diffusion to the spatial and temporal evolution of the solution.

In addition to the turbulent-flow test cases, the scheme has been analytically and numerically checked for stability and accuracy. These validation studies have shown:

(i) that the scheme, in its basic form without added numerical diffusion, is second-order accurate in space, first- or second-order accurate in time;
(ii) that the various modes of numerical diffusion preserve this order of accuracy;
(iii) that the stability zones of these smoothing modes correspond to their intended range of applicability;
(iv) and that the union of these stability zones covers the entire range of velocity directions.

The numerical scheme having been validated in laminar flow, the discrepancies observed in turbulent flow between numerical solutions and experimental results are thought to be mainly caused by a lack of generality of turbulence models, along with uncertainties in the description of experimental data.

Therefore, the overall assessment of the scheme's behaviour authorizes its integration into a more complete computational code, built around a Navier–Stokes solver, which will not be impeded by the computational effort required to model the endwall boundary layers.

REFERENCES

1. Wang KC. On the determination of the zones of influence and dependence for three-dimensional boundary-layer equations. *Journal of Fluid Mechanics* 1971; **48**(2):397–404.
2. Cousteix J, Houdeville R. Singularities in three-dimensional turbulent boundary layer calculations and separation phenomena. *AIAA Journal* 1981; **19**(8):976–985.
3. Houdeville R, Mazin C, Corjon A. Méthode de caractéristiques pour le calcul de couches limites tridimensionnelles. *La Recherche Aérospatiale* 1993; **1**:37–49.
4. Houdeville R, Bardoux P, Moreux V. 3D boundary layer computations on wing-pylon-nacelle configuration. *Workshop on Aspects of Airframe Engine Integration for Transport Aircraft*. Braunschweig, Germany, March 1996 (ONERA TP 1996-75): 1–16.
5. Patankar SV. *Numerical Heat Transfer and Fluid Flow*. Hemisphere, 1980.
6. Zang Y, Street RL, Koseff R. A non-staggered grid, fractional step method for time-dependent incompressible Navier–Stokes equations in curvilinear coordinates. *Journal of Computational Physics* 1994; **114**:18–33.
7. Cebeci T, Smith AMO. *Analysis of Turbulent Boundary Layers.* Academic Press, 1974.
8. Cooke JC. The boundary layer of a class of infinite yawed cylinders. *Proceedings of Cambridge Philosophical Society* 1950; **46**:645–648.
9. Monnoyer de Galland F. Calculation of three-dimensional attached viscous flow on general configurations using second-order boundary-layer theory. *Zeitschrift für Flugwissenschaften und Weltraumforschung* 1990; **14**: 95–108.
10. Buisine D, Horri-Naceur J. A fast hyperbolic scheme for the 3D boundary layer equations – introduction of a particular numerical viscosity. In *First European Conference on Turbomachinery – Fluid Dynamic and Thermodynamic Aspects*. Erlangen, Germany, March 1995: 95–109.
11. Horri-Naceur J. *Schéma numérique pour la résolution des équations de la couche limite tridimensionnelle – Applications*. PhD thesis, Université des Sciences et Technologies de Lille, January 2000.
12. Littell HS, Eaton JK. Turbulence characteristics of the boundary layer on a rotating disk. *Journal of Fluid Mechanics* 1994; **266**:175–207.

